Squeal measurement with 3D Scanning Laser Doppler Vibrometer: handling of the time varying system behavior and analysis improvement using FEM expansion

G. Martin[1], E. Balmes[1,2], G. Vermot des Roches[1], T. Chancelier[3]
[1] SDTools, 44 Rue Vergniaud, 75013 Paris, France
[2] ENSAM, PIMM, 151 Bld de l'Hopital, 75013 Paris, France
[3] Chassis Brakes International, Drancy, France
e-mail: **martin@sdtools.com**

Abstract

In the presence of squeal, Operational Deflection Shapes (ODS) are classically performed to analyze behavior. A simple numeric example is used to show that two real shapes should dominate the response. This justifies an ad-hoc procedure to extract main shapes from the real brake time measurements. The presence of two shapes is confirmed despite variations with wheel position and reproducibility tests. To obtain a high spatial density measurement, 3D Scanning Laser Doppler Vibrometer is interesting but leads to iterative measurements on a time-varying system. An algorithm to merge sequential measurement and extract main shapes is detailed. Even with a high-density 3D SLDV measurement, shapes characterizing the squeal event are still only known on accessible surfaces. Minimum Dynamic Residual Expansion (MDRE) is thus finally used to estimate motion on a full FE mesh which eases interpretation and highlights areas where the test and the model contain errors.

1 Introduction

Squeal being an undesired condition, its appearance is never predicted by initial design models, when they exist, and experiments are needed to understand the exact conditions of occurrence. Two major techniques are classically used to perform vibration measurements on brake systems: accelerometer measurements and 3D Scanning Laser Doppler Vibrometer measurement. The specificities of each measurement techniques are reminded in Table 1.

	Accelerometer	3D-SLDV
Synchronous measurement	Yes	No
Setup time	Long	Acceptable
Wireframe density	Low	High
Without contact	No	Yes
Rotating parts	No	Yes
Hidden parts	Yes	No

Table 1: Characteristics of accelerometer and 3D-SLDV measurements

The 3D-SLDV is interesting because the setup time is reasonable, it is without contact, and it can offer a high number of measured points. However, only visible parts can be measured. Some accelerometers can be used to add missing information but this still does not include tight areas or junctions. The main

disadvantage of the 3D-SLDV to measure a squeal phenomenon is that measurements are sequential. This is a problem because as will be highlighted in section 3, brake squeal is a time varying phenomenon.

The first objective of this study was to propose an experimental strategy to extract shapes that characterize the limit cycle associated with a squeal occurrence. To propose and adequate strategy it is first necessary to have prior knowledge of the expected properties. Section 2 uses a simple numerical model [1] to illustrate that the shapes associated with squeal instabilities are expected to be dominated by the combination of two real modes with contributions that may be quite sensitive to changes.

Knowing that a limit cycle is expected to be composed of a time varying combination of fixed shapes, Section 3 exploits time-frequency analyses of experimental measurements to demonstrate that indeed two real shapes dominate the response and have variations that are coherent with the changes due wheel position. A reproducibility test further demonstrates that, while different experiments can lead to notable frequency shifts, the shapes underlying the limit cycle are fairly constant. This first analysis is performed using test on the drum brake test bench shown in figure 1 left.

Figure 1 : Experimental setups. Left drum-brake used for section 3.
Right : disk-brake used for sections 4-5.

Because of the low spatial density, the accelerometer measurements can be difficult to exploit. The second objective of this paper is thus to present the strategy developed to extract principal shapes from 3D-SLDV measurements. The algorithm is described in Section 4 and applied on the brake shown in figure 1 right.

Finally, despite a quite high spatial resolution of the laser measurement, many parts are not accessible to the measurement. As a result, using mode shape expansion techniques to estimate the full FE response from measurements appears as a necessity to provide understanding of inconsistencies between model and test and thus pave the way for the proposition of modifications. The Minimum Dynamic Residual (MDRE) method [2] is applied in Section 5 to illustrate the potential uses. It is shown that expanded shapes give better understanding of the brake motion and that distribution of the residual energy after expansion gives insight on modeling errors.

2 Expected shapes in a squeal event: a simple example

To motivate the procedure used to analyze shapes during a squeal event, a simple numeric example is detailed here. As motivated in [1], the complex mode shapes come from the linearization of the model around a chosen state (pressure, velocity…). The linearized model provides a system of the form

$$[M]\{\ddot{q}(t)\} + [C]\{\dot{q}(t)\} + [K_s + K_u]\{q(t)\} = \{f_{ext}(t)\} \qquad (1)$$

where $q, \dot{q}$ et $\ddot{q}$ are displacements, velocities and acceleration, M, C, K are respectively the mass, damping and stiffness matrices supposed constant. The stiffness matrix can be decomposed in a symmetric part K_s, coming from the elastic properties of each components and the linearization of the normal contact loads and a non-symmetric part K_u linked to the fluctuation of the tangential loads induced by the fluctuation of the normal loads. It is classical to project the system in the real mode basis $[\Phi]$, found by solving the system with $[C] = 0$ and $K_u = 0$ (which is equivalent to consider a friction coefficient $\mu = 0$). Projected in this basis, the complex modes are solution of

$$\left(\begin{bmatrix} \omega_j^2 \end{bmatrix} + [\Phi^T K_u \Phi] + \lambda_j [\Phi^T C \Phi] + \lambda_j^2 [I]\right)\{\psi_{jR}\} = 0 \qquad (2)$$

with restitution on the full set of Degrees Of Freedom (DOFs) computed using $\{\psi_j\} = [\Phi]\{\psi_{jR}\}$.

The simplified brake shown in Figure 2 is used as an illustration. The disc (blue) and the backplate (yellow) are made of steel and the friction (green) is made of an orthotropic softer material, about 5GPa with an additional Rayleigh damping (see the introduction of [1] for details). The model is clamped at 4 locations at the interface between the backplate and the friction (similar to the one circled in the figure).

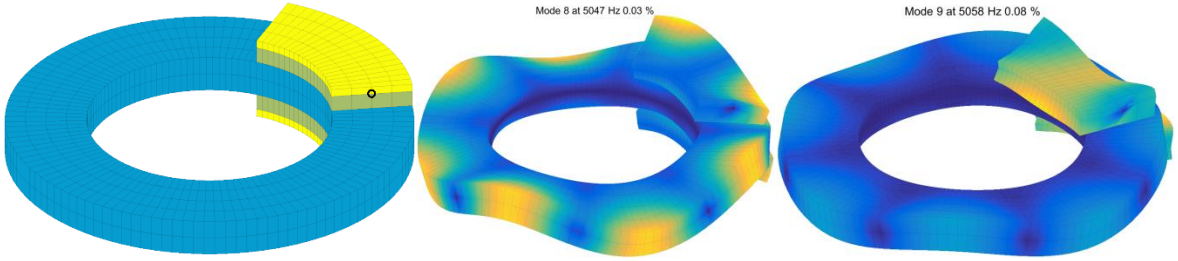

Figure 2 : Simple brake model geometry (left) and real mode shapes #8 and #9. (right)

This model has an unstable (negative damping) complex mode at 5050Hz which corresponds to the interaction between the two real modes #8, with a mostly out-of-plane deformation, and #9 with mostly a deformation of the pads sliding on the disc.

To confirm that the complex mode shape mainly comes from the interaction between the two real shapes, the friction coefficient is swept from 0 to 0.2 (not a physical value but still relevant for the interpretation). The left of Figure 3 shows that the complex modes #8 and #9 are stable at first (as indicated by the red dots). Then with the increase of the friction coefficient, mode #8 becomes unstable, while the damping of mode #9 increases.

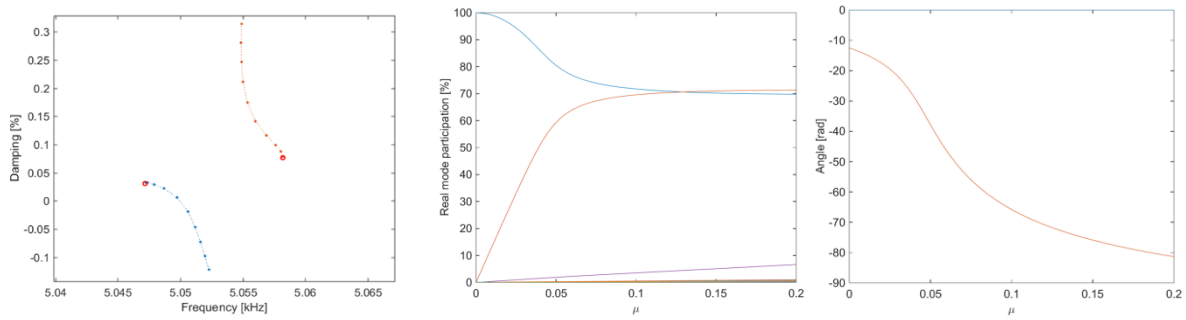

Figure 3 : Evolution of complex modes with the friction coefficient: roots (left), real mode participation to the complex mode #8 (middle) and phase between real modes #8 and #9 (right)

From (2), it is possible to look at the evolution of the real mode participation (ψ_{jR}) of each modal DOF with the normalization $\|\psi_R\| = 1$. Figure 3 center thus shows the participation of the real modes to complex mode #8, which become unstable, evolves from 100% of real mode #8 (blue line) to 70% of real mode #9 (red line) and 70% of real mode #8. Figure 3 illustrates the significant evolution of the phase relation between contributions of real modes #8 and #9 to complex mode #8.

To evaluate the pertinence to use only two real modes to interpret the unstable modes, equation (2) is reduced on the 2 real mode shapes #8 and 9, leading (with the assumption of modal damping) to

$$\left(\begin{bmatrix}1 & 0\\ 0 & 1\end{bmatrix}\lambda_j^2 + \begin{bmatrix}2\zeta_8\omega_8 & 0\\ 0 & 2\zeta_9\omega_9\end{bmatrix}\lambda_j + \begin{bmatrix}\omega_8^2 & 0\\ 0 & \omega_9^2\end{bmatrix} + \begin{bmatrix}k'_{11} & k'_{12}\\ k'_{21} & k'_{22}\end{bmatrix}\right)\{\psi_{jR}\} = 0 \qquad (3)$$

The comparison between the system reduced on the two real modes on the one hand and on all real modes on the other hand is provided by Figure 4. The accuracy of frequencies is not as good with only two shapes, but the coupling still occurs and the damping computation is almost unchanged.

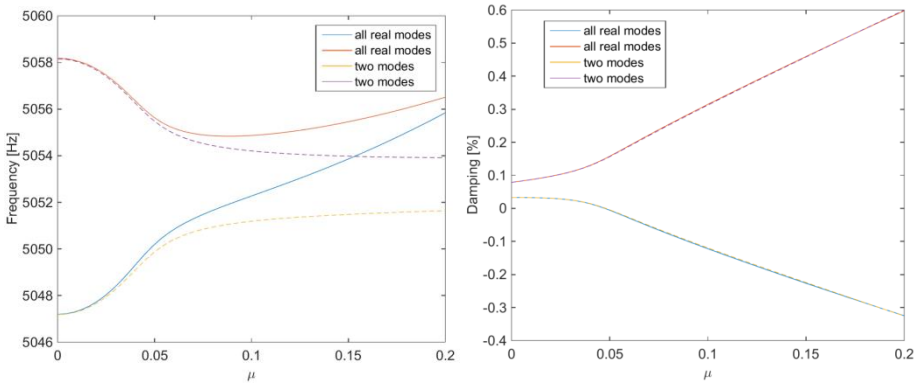

Figure 4 : Complex modes frequency (left) and damping (right) for variable friction coefficient. Reduction on two real modes (dashed lines) and on all real modes (full lines).

The common practice in presence of coupled modes is to try separating the frequencies. Doing so on the two shape reduced model, by moving away their frequencies with the same percentage (modifying k_1, k_2, c_1, c_2 but not the non-symmetric stiffness part), results in the evolution of the complex frequencies and damping shown in Figure 5. As mode #9 damping decreases, mode #9 one increases until it is no longer unstable. The dot lines represent the values of the frequencies $f_8\, f_9$ and dampings $\zeta_8\, \zeta_9$. When the frequencies are moved away, the influence of the coupling stiffness decreases, and the mode parameters converge toward the ones without coupling at all.

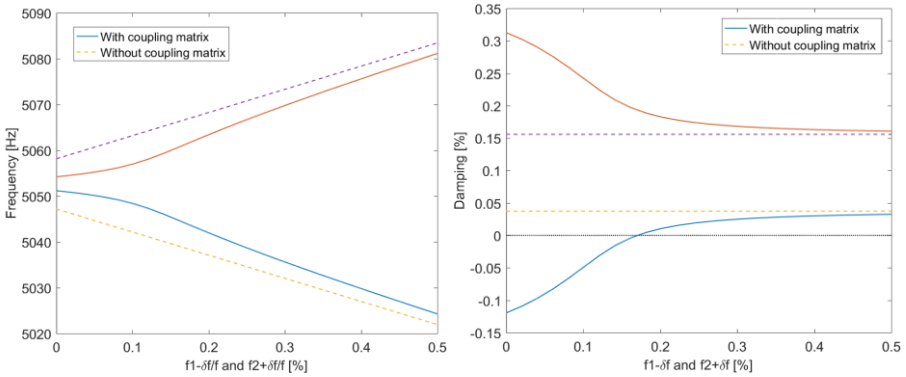

Figure 5 : Complex mode frequency and damping for varying frequency shift of real modes #8 and #9

3 Time frequency analysis

With the objective of extracting the characteristics of a limit cycle, it is first necessary choose a strategy to extract shape information. The test case used for illustration is the drum brake of figure 1 left. The measurement is performed using 38 accelerometers measured simultaneously. The measurement geometry was built [2] from the numerical mode shapes, using the MSeq algorithm [3], to distinguish the modes in a frequency band around 900Hz. In the picture, the drum was removed to see the internal instrumentation.

For this brake, a low frequency squeal occurrence (about 900Hz) has been found on vehicle and needed to be reproduced on bench for further analysis.

To analyze the evolution of the squeal with time, the Gabor transform is used to decompose the signal in the time-frequency domain. It consists in a Short Time Fourier Transform where at each time step, the signal is convolved with a Gaussian window whose standard deviation $\sqrt{\Delta t^2}$ is used to choose the compromise between time and frequency resolution, fixed by the Heisenberg-Gabor equality $\sqrt{\Delta t^2}\sqrt{\Delta f^2} = \frac{1}{4\pi}$.

The Gabor transform is applied to the measurement on an arbitrary sensor with a very good frequency resolution $\sqrt{\Delta f^2} = 0.5Hz$ which induces a quite poor time resolution $\sqrt{\Delta t^2} = 0.1592s$. This is acceptable because the squeal behavior evolution with time is slow. Figure 6 left shows that during the squeal, the frequency shifts between 906Hz and 913Hz. Three time slices on the right of the figure also highlight the amplitude evolution of the main resonance. A smaller peak of amplitude, constant in frequency at 900Hz, is present for each measurement and is due to an harmonic of the power supply of the bench (50Hz). It is interesting to note that this choice is notably different from earlier practice which used much shorter buffers in favor of a better time resolution.

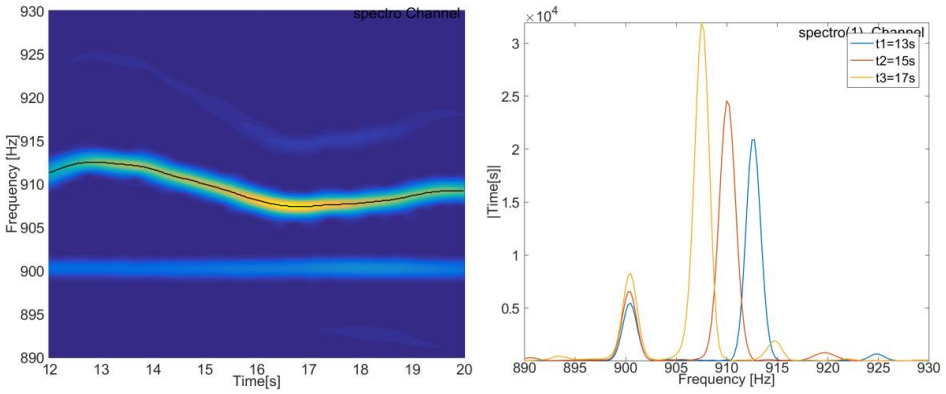

Figure 6 : Gabor transform of a squeal measurement (left), time slices (right)

To evaluate in detail the evolution of the behavior, at each instant t, the frequency where the amplitude is maximum $f_{max}(t)$ is found, and the corresponding shape $\{y(f_{max}(t), t)\}$ is extracted. All these shapes are concatenated and real plus imaginary parts are decomposed with the Singular Value Decomposition providing sorted real shapes $\{U_j\}$

$$[F] = [\Re(\cdots y(f_{max}(t), t)\cdots)\ \Im(\cdots y(f_{max}(t), t)\cdots)]_{NS\times 2NT} = \sum_j \{U_j\}\sigma_j\{V_j\}^T \qquad (4)$$

with NS the number of sensors and NT the number of time steps.

The family $[\cdots y(f_{max}(t), t)\cdots]$ can then be decomposed on these real shapes, leading to

$$[\cdots y(f_{max}(t), t)\cdots] \approx \sum_j \{U_j\}_{NS\times 1}\{a_j(t)\}_{1\times NT} \qquad (5)$$

with $a_j(t) = \sigma_j \times (v_j(t) + iv_j(t + NT))$.

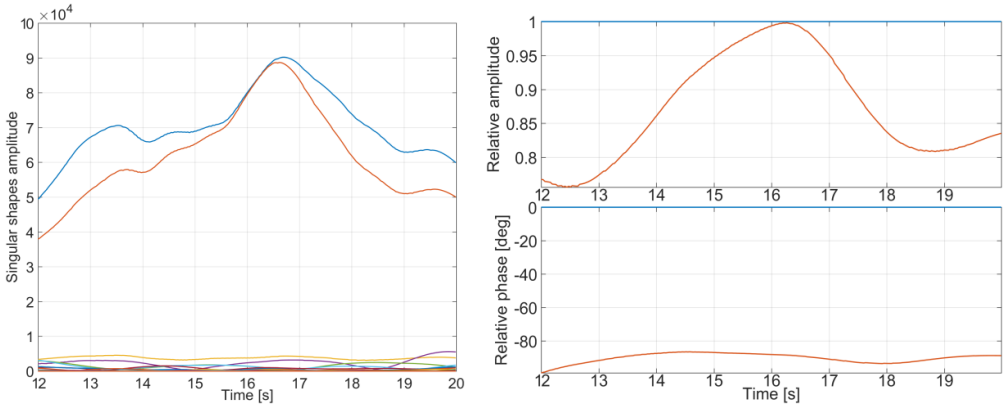

Figure 7 : Time evolution of the main real shapes $|a_j(t)|$ (left) and relative evolution between the two main shapes $a_2(t)/a_1(t)$.

Figure 7 left shows the time evolution of $|a_j(t)|$ and it is clear that the limit cycle shape has only two significant amplitudes and is thus well represented the by two main real shapes $[U_1 U_2]$. The relative evolution between the two main shapes $a_2(t)/a_1(t)$ is analyzed on the right and show an amplitude ratio in the range 0.75-1 and a low phase evolution between -85° and -100°. Thus the limit cycle, despite the evolution of the complex shape, stays in the same subspace in an analogous way than the numerical result illustrated in section 2.

It is also important to evaluate reproducibility. For this purpose, a second squeal event has been measured a day after the first measurement, leading to potential evolution of parameters such as pressure map, relative component placement or temperature. The time-frequency evolution of this second measurement and for the same sensor is shown on Figure 8. A quite important frequency shift is also found from 917Hz to 925Hz and is in average more than 10Hz higher than the first one.

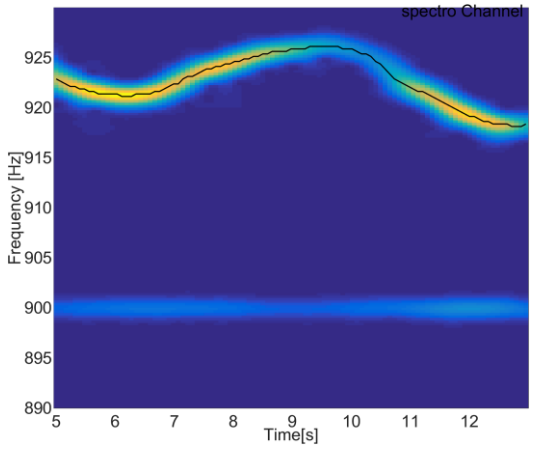

Figure 8 : Gabor transform of the second squeal measurement.

The family containing the two measurement, normalized to have the same weight

$$[y(t)] = \left[\frac{[\cdots y_1(f_{max}(t),t)\cdots]}{\|\cdots y_1(f_{max}(t),t)\cdots\|} \; \frac{[\cdots y_2(f_{max}(t),t)\cdots]}{\|\cdots y_2(f_{max}(t),t)\cdots\|}\right] \qquad (6)$$

is used and decomposed as in (4) and (5). The evolutions of the amplitudes $|a_{j,1}(t)|$ and $|a_{j,2}(t)|$, related to the common main real shapes shown in Figure 9. The predominance of the two main real shapes is a bit less clear than when the first measurement was decomposed alone (see Figure 7 left), but still there.

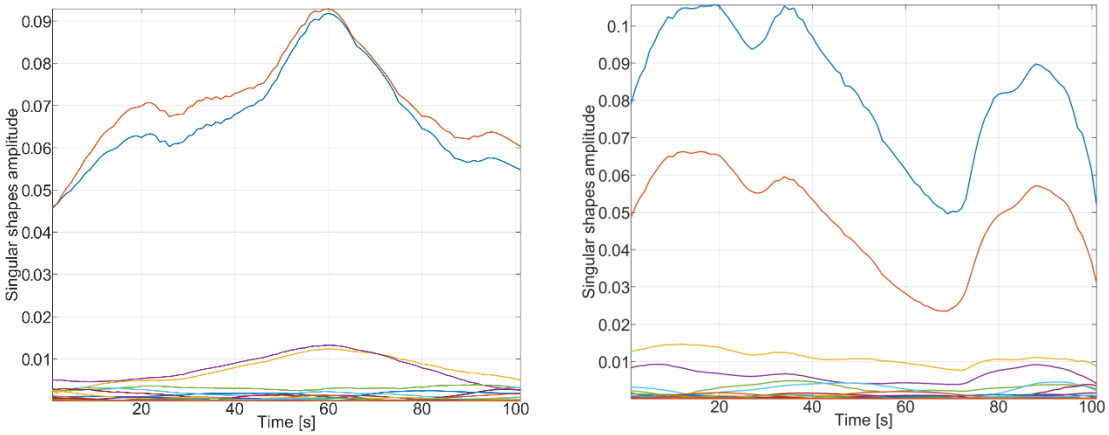

Figure 9 : Time evolution of the common main real shape amplitudes for the first measurement $|a_{j,1}(t)|$ (left) and the second measurement $|a_{j,2}(t)|$ (right).

4 Extraction of principal shapes from laser measurements

Tests limited to accelerometers have a very limited resolution. 3D-SLDV measurements allow a higher spatial density but lead to sequential measurements. The objective of this section is thus to introduce a methodology for shape extraction in this context. The test case is the disk brake of figure 1 right. The measurements have been performed using the Polytec Scanning Laser Doppler Vibrometer PSV500 using the test geometry visible in Figure 11. This system presents a squeal occurrence at about 4250Hz. To extract the two main shapes from the sequential measurements, three reference monoaxial accelerometers have been disposed on the structure as reference: one on the caliper, one on the anchor bracket and one on the arm.

In order to aggregate the sequential measurements, the hypothesis used is that a subspace of response shapes of dimension two remains constant during the squeal.

For each point i of the wireframe presented in the introduction, a time measurement is performed (0,1s) containing three measured signals Xi, Yi, Zi at the scanned point and reference accelerometers

$$\begin{matrix} x^i(t) \\ y^i(t) \\ z^i(t) \\ \vdots \\ \left\lfloor a_{Ref}(t) \right\rfloor_{i\in[1,N_{laser}]} \end{matrix} \qquad (7)$$

For each laser position i, the two main real shapes $[\Phi_1^i \Phi_2^i]$ are extracted using the SVD (4). To concatenate each measured point, two main shapes at the references $\left[\phi_1 \phi_2\right]_{|ref}$ are needed. These are obtained using again an SVD on the restriction at reference accelerometers of all the previously extracted main shapes

$$[\Phi_1^1 \Phi_2^1 \ldots \Phi_1^i \Phi_2^i \ldots \Phi_1^N \Phi_2^N]_{|ref} = \sum_j \left\{\phi_j\right\}_{|ref} \sigma_j \{V_j\}^T \qquad (8)$$

Finally, for each measured point i, the objective is to find the best linear combination $\left[\lambda^i\right]$ of $[\Phi_1^i \Phi_2^i]$, that minimizes the Euclidian distance with the target shape at references $\left[\phi_1 \phi_2\right]_{|ref}$

$$[\lambda^i]=[\Phi_1^i \Phi_2^i]^+_{|ref}[\phi_1 \phi_2]_{|ref} \quad (9)$$

and the concatenation for each point of

$$\left[\tilde{\phi}_1^i \tilde{\phi}_2^i\right] =[\Phi_1^i \Phi_2^i][\lambda^i] \quad (10)$$

forms the two main shapes.

This procedure has been applied to the 3D-SLDV measurement of the brake disc presented in introduction. Around 4250Hz, the two main shapes shown in Figure 10 have been extracted.

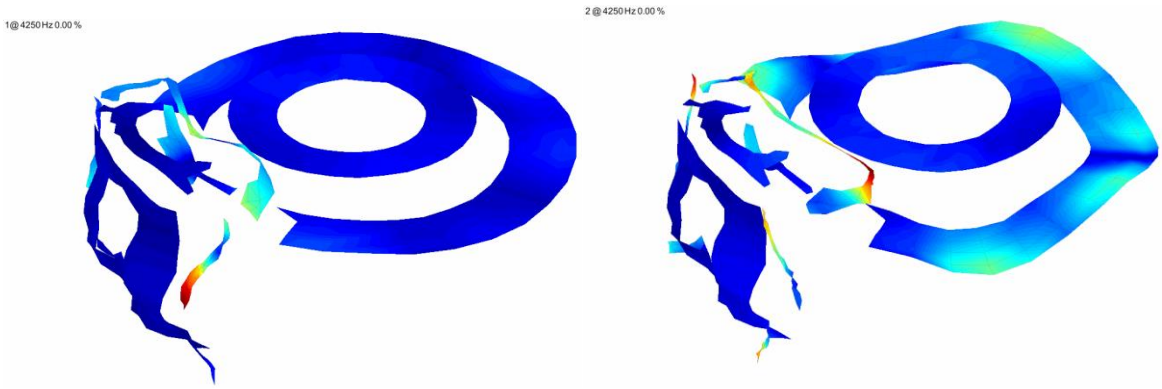

Figure 10 : Visualization of the two main shapes extracted from all the sequential time measurement with the proposed method

The first shape shows mainly a deformation of the bracket. The second shape shows another deformation of the bracket with a deformation of the disc.

5 Expanding the results to full FEM size

Despite the high spatial resolution of the 3D-SLDV measurement, information such as hidden parts or interfaces between components are missing. Using a FEM to perform expansion is useful for two main reasons: it evaluates the deformations at all FEM DOFs which helps in analyzing the shapes and depending on the used algorithm, it can highlight areas where the FEM is doubtful which orients model updating procedures.

As illustrated in Figure 11, the test wireframe has been constructed in two parts: one in the direct view to measure the disc, a part of the caliper and a part of the anchor bracket and one through the mirror to measure the remaining parts of the caliper and the anchor bracket. The experimental wireframe geometry is overlaid with the FEM and clearly illustrates the missing areas.

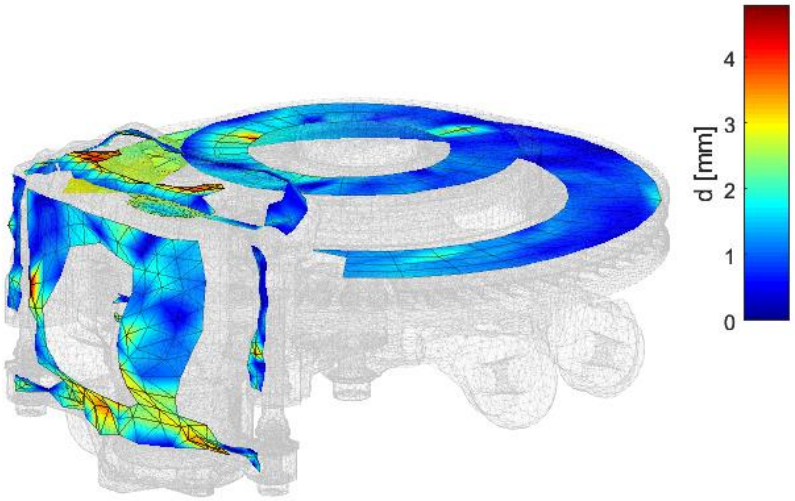

Figure 11 : Measurement wireframe on top of the FEM

The two shapes obtained from the exploitation of the limit cycle measurements are used to perform expansion with a FEM. The MDRE [4] algorithm is used, which consists in finding the shape $\{\hat{\phi}\}$ that minimizes the weighted sum of two energies: ϵ_{Mod} linked to the residual force $Z(\omega)\{\hat{\phi}\} = \{R_L(\omega)\}$ (not zero because the model is not exact) and ϵ_{Test} linked to the measurement error (the error between the measured shape and the observation at sensors of $\{\hat{\phi}\}$). The cost function is then written

$$J = \epsilon_{Mod} + \gamma\epsilon_{Test} \tag{11}$$

with γ the weighting between the two errors. *In more* details, to measure the residual force, the static displacement which it engenders is computed *as*

$$\{R_D(\omega)\} = [K]^{-1}\{R_L(\omega)\} = [K]^{-1}\, Z(\omega)\{\hat{\phi}\} \tag{12}$$

and the deformation energy linked to this residual displacement is the error of model

$$\epsilon_{Mod} = \{R_D(\omega)\}^H[K]\{R_D(\omega)\} \tag{13}$$

To express the measurement error, the expanded shape is observed at sensors using the observation matrix $[c]$ and compared with the measured shape using the classical Euclidian norm

$$\epsilon_{Test} = \left([c]\{\hat{\phi}\} - \{y_{Test}\}\right)^T \left([c]\{\hat{\phi}\} - \{y_{Test}\}\right) \tag{14}$$

From these two errors, the cost function can be put in a matrix form (see [4] and [2]) and thus the expanded mode shape can be found directly for each value of γ.

Nevertheless, full resolution of MDRE is generally not accessible [5], so that the reduction proposed in [2] is a major contribution. The FEM is reduced on a basis combining the response to unit loads at sensors, for the result to be at least as good as the static expansion, and the free modes of the structure (considering the friction coefficient equals to zero), for the expansion to be exact if the model matches perfectly the measurements. This family of shapes is orthonormalized with respect to mass and stiffness matrices, leading to the basis

$$[T] = \left[[\Phi]_{NM}[\Phi^{\perp}]\right] \tag{15}$$

with $[\Phi]_{NM}$ the free mode shapes and $[\Phi^{\perp}]$ the part of the response to unit loads at sensors that is orthogonal to the free modes (this part will be called later enrichment).

Furthermore, this model reduction can be useful if the expansion is used in combination with an updating procedure, to speed up the parametrized studies. It also permits a quick evaluation of the MDRE result with several values of the parameter γ which allows more or less measurement error.

Rather than absolute measurement and model errors, relative errors are introduced to ease interpretation of the role of parameter γ. The relative measurement error is defined by

$$\epsilon_{Test}^{R} = \frac{\sqrt{\epsilon_{Test}}}{\|y_{Test}\|} \tag{16}$$

and the relative model error by

$$\epsilon_{Mod}^{R} = \frac{\epsilon_{Mod}}{\{\hat{\phi}\}^{T}[K]\{\hat{\phi}\}} \tag{17}$$

Because of the chosen reduction basis, the DOFs q_R can be decomposed in those linked to the free modes q_M and those linked to the enrichment $q_{M^\perp}$. In this basis, the stiffness matrix is diagonal with first the mode pulsations ω_M^2 and then the pseudo-pulsations $\omega_{M^\perp}^2$. From this property, the model error can be decomposed in the part linked to the free modes and the part linked to the enrichment

$$\epsilon_{Mod} = \{R_D\}_{|M}{}^{T}\begin{bmatrix}\ddots & & \\ & \omega_{\mathrm{M}}^2 & \\ & & \ddots\end{bmatrix}\{R_D\}_{|M} + \{R_D\}_{|\mathrm{M}^\perp}{}^{T}\begin{bmatrix}\ddots & & \\ & \omega_{\mathrm{M}^\perp}^2 & \\ & & \ddots\end{bmatrix}\{R_D\}_{|\mathrm{M}^\perp} \tag{18}$$

Several expansions with an increasing γ from 1 to 1e10 have been performed on the disc brake test case. The evolution of the relative measurement and model errors is shown in Figure 12.

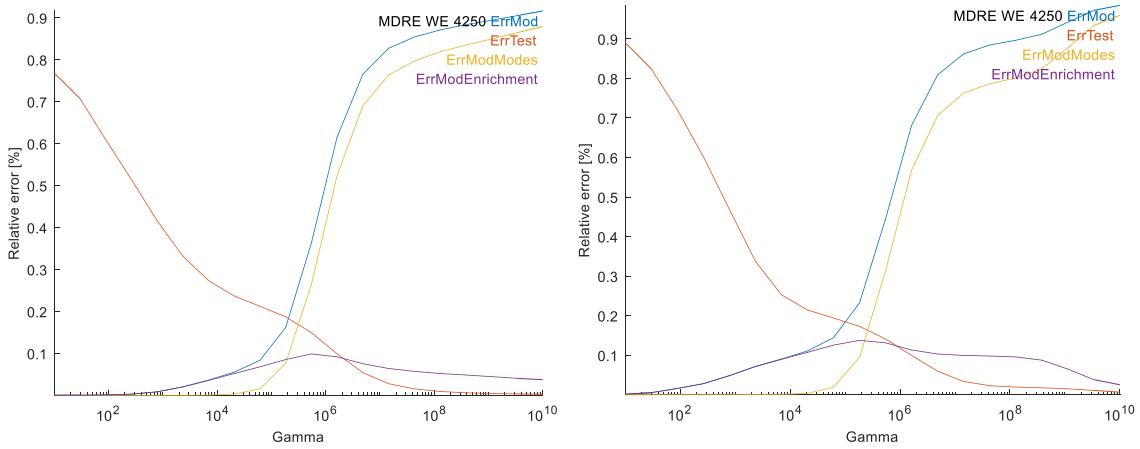

Figure 12 : Evolution of relative model and measurement error with γ. Left: first main shape, right: second.

For a very low value of $\gamma = 1$, the relative model error is really low but the expanded shape does not match the measurements. When increasing the value of γ, the measurement error decreases with at first an incresing model error linked to the enrichment (up to $\gamma = 10e5$). Then, the measurement error continues to decrease but with a strong increase of the model error linked to the free modes: to represent the measurement well, the free modes are used but do not satisfy well the mechanical equilibrium of the model. The free mode subspace seems thus relevant but does not have the good frequency distribution.

Choosing an intermediate γ (5e+05), the expanded mode shapes are show in Figure 13.The first one is dominated by the deformation of the right column and the right side of the caliper. The second shape is mostly a deformation of the whole caliper and again the right column. The analysis of the squeal behavior

with the expanded shapes is simpler than with only the deformations at sensors. It can help providing modification propositions to impact the phenomenon.

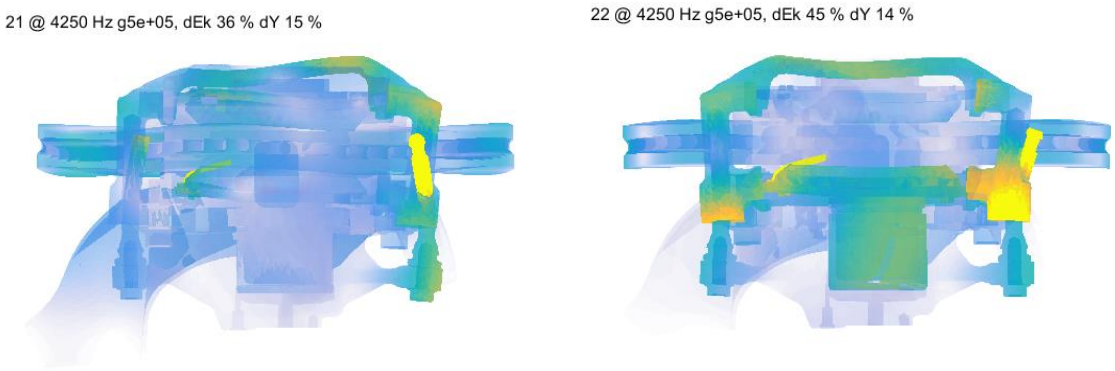

Figure 13 : Expansion result for the two extracted experimental shapes form the limit cycle measurements.

The expansion can also be used to analyze the model quality. Indeed, the energy distribution coming from the residual forces shows areas of the model where the mechanical equilibrium is poor. This residual energy can be split in two: the residual energy related to the free mode shapes, and the residual energy related to the enrichment shapes.

Figure 14 shows that the residual energy related to the enrichment shapes is mostly a concentration of energy near the sensor locations

Figure 14 : Model error on the enrichment shapes

Figure 15 shows residual energy distribution on the free mode shapes. This energy is more global with nevertheless several concentration areas: in the sliding contact between the pad and the disc (A), at each contact between the pad and the caliper (B) and between the columns and the caliper (C). Using these residual energy maps helps defining a relevant parametrization of the model to perform model updating if needed.

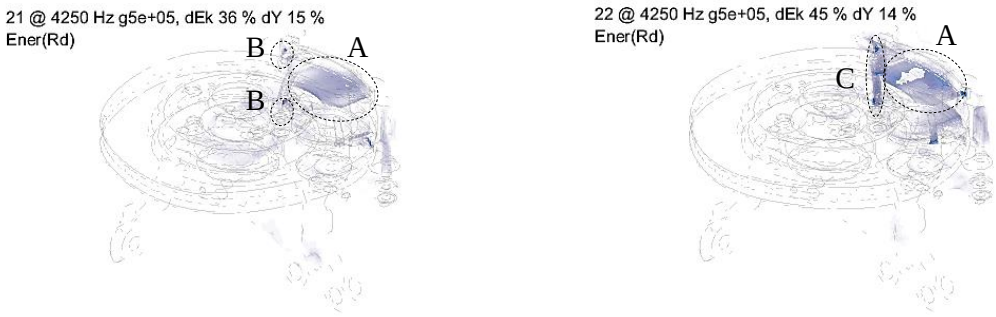

Figure 15 : Model error on the free mode shapes

6 Conclusion

This study showed that the interpretation of the squeal behavior as an interaction between two real shapes makes sense, not only numerically but also experimentally. The reproducibility of the phenomenon, despite frequency shifts, is good when the subspace is compared instead of the complex shapes directly: the limit cycle lies in a two-dimensional subspace with a slow variation of relative amplitude and phase. The time/frequency analysis strategy retained is very simple and more advanced techniques such as the Hilbert transform could be considered [6]. Tracking of modes during the cycle and before the squeal instability would be a useful complement to the test performed here. It would correspond to force appropriation and could be coupled to auto-resonance techniques [7].

The two-dimensional subspace is sufficiently stable to allow a piecewise reconstruction combining reference sensors and 3D-SLDV measurements. This leads to field measurements of squeal shapes, but still only measures accessible surfaces and thus fail to give indications about the behavior of junctions.

Finally, the expansion of the two shapes extracted from the limit cycle measurements provides a fully detailed estimation of the test shapes. The proposed reduction methodology enables practical studies on industrial models and the results can be interpreted in terms of shapes of interest and possibly as a basis to localize errors to be used in model updating analysis. Combining expansion and updating is a clear perspective of this work.

References

[1] G. Vermot Des Roches, “Frequency and time simulation of squeal instabilities. Application to the design of industrial automotive brakes,” Ph.D. thesis, Ecole Centrale Paris, CIFRE SDTools, 2011.

[2] G. Martin, “Méthodes de corrélation calcul/essai pour l’analyse du crissement,” Ph.D. thesis, CIFRE SDTools, Arts et Metiers ParisTech, Paris, 2017.

[3] E. Balmes and others, “Orthogonal Maximum Sequence Sensor Placements Algorithms for modal tests, expansion and visibility,” *IMAC*, vol. 145, p. 146, 2005.

[4] E. Balmes, “Review and Evaluation of Shape Expansion Methods,” *IMAC*, pp. 555–561, 2000.

[5] N. Nifa, “Solveurs performants pour l’optimisation sous contraintes en identification de paramètres,” Ph.D. thesis, Université Paris-Saclay, 2017.

[6] M. Feldman, *Hilbert Transform Applications in Mechanical Vibration: Feldman/Hilbert Transform Applications in Mechanical Vibration*. Chichester, UK: John Wiley & Sons, Ltd, 2011.
[7] S. Davis and I. Bucher, "Automatic vibration mode selection and excitation; combining modal filtering with autoresonance," *Mech. Syst. Signal Process.*, vol. 101, pp. 140–155, Feb. 2018.